Journal of Materials Chemistry A

PAPER

View Article Online
View Journal | View Issue

Cite this: J. Mater. Chem. A, 2017, 5, 10895

Design of ultralong single-crystal nanowire-based bifunctional electrodes for efficient oxygen and hydrogen evolution in a mild alkaline electrolyte†

Ge Li,[a] Xiaolei Wang,*[ab] Min Ho Seo,[c] Sahar Hemmati,[a] Aiping Yu[a] and Zhongwei Chen*[a]

Received 29th March 2017
Accepted 4th May 2017

DOI: 10.1039/c7ta02745a

rsc.li/materials-a

Rational design of bifunctional electrodes that efficiently pair oxygen evolution reaction (OER) and hydrogen evolution reaction (HER) in a single system is critical for electrocatalytic pure oxygen and hydrogen generation and overall water splitting. Herein, we report a novel biomimetic architectural design and development of 3D flexible electrodes with high electrocatalytic activity and durability in a mild alkaline system. Benefiting from the ultralong single-crystal Co-doped ZnO nanowires densely and *in situ* grown on highly conductive carbon fabric, the novel material and unique composite electrode architecture favor the direct electrochemical water splitting process over the conventionally fabricated electrodes by providing abundant active sites, efficient electron transfer pathways, and sufficient gas exchange channels. A low overpotential of 360 and 275 mV is required to reach a current density of 10 mA cm^{-2} for OER and HER, respectively. When these thick electrodes are used as electrocatalysts for both anode and cathode in an overall water electrolyzer, a low cell voltage of 1.90 V and 2.06 V is required to reach a current density of 4.0 and 10.0 mA cm^{-2}, respectively, with an extremely long durability. Such a single-cell prototype exhibiting superior performance to noble metal-based precious catalyst counterparts holds great promise in future practical applications for pure hydrogen generation.

Introduction

Direct electrochemical water splitting for sustainable production of high-purity hydrogen and oxygen has been regarded to be crucial to enable efficient energy storage and carbon dioxide-free energy utilization technologies including fuel cells and rechargeable metal–air batteries.[1–4] Theoretically, a voltage of 1.23 V is required for electrochemical water splitting, while a much higher value (>1.9 V) is often applied for the practical electrolysis process in highly concentrated electrolytes, since both hydrogen evolution reaction (HER) and oxygen evolution reaction (OER) are thermodynamically uphill and kinetically sluggish.[5,6] Electrocatalysts are often applied to overcome large overpotentials and realize less energy-intensive processes. So far, platinum (Pt) and iridium oxide (IrO_2) have been widely accepted as the most active electrocatalysts for HER in acidic electrolytes and OER in basic electrolytes, respectively. The corresponding electrolyzer exhibits a low voltage of ~1.5 V to achieve the typical high current of 10 mA cm^{-1} during the water splitting.[7,8] Unfortunately, the widespread use of these precious metal-based catalysts is still hindered by their scarcity and electrochemical instability.[9–12]

As alternatives, high-performance HER and OER catalysts using earth-abundant elements hold great promise to efficiently catalyze water electrolysis and effectively reduce the cost. For example, cobalt phosphate,[13] perovskite oxides,[14,15] transition metal oxides[16] and hydroxides[17] have been widely reported for OER, while nickel-molybdenum alloy,[18,19] Co–C–N complex,[20,21] transition metal dichalcogenides[22,23] and phosphides[24] have been extensively studied for HER. Although these catalysts exhibit comparable or even superior catalytic activity to precious metal-based catalysts, their catalytic activities have to be realized in the same highly concentrated electrolyte. More importantly, it is extremely difficult and complex to directly integrate two half-reactions in a single system due to the mismatch of electrolytes with different pH values, where these catalysts could remain stable and most active.[7,25,26] In this context, the development of novel multi-functional electrocatalysts with high activity and excellent stability that efficiently pair HER/OER processes, especially in a mild environment, where the electrolyte carbonation caused by the reaction of CO_2 with highly concentrated alkaline

[a]Waterloo Institute for Nanotechnology, Department of Chemical Engineering, University of Waterloo, 200 University Avenue West, Waterloo, Ontario N2L 3G1, Canada. E-mail: zhwchen@uwaterloo.ca; xiaolei.wang@uwaterloo.ca

[b]Department of Chemical and Materials Engineering, Department of Mechanical and Industrial Engineering, Concordia University, 1455 De Maisonneuve Blvd. West, Montreal, Quebec H3G 1M8, Canada

[c]Hydrogen and Fuel Cell Center for Industry, Academy and Laboratories, New & Renewable Energy Research Division, Korea Institute of Energy Research, 20-41 Sinjaesaengeneogi-ro, Haseo-myeon, Buan-gun, Jellabuk-do 56332, South Korea

† Electronic supplementary information (ESI) available. See DOI: 10.1039/c7ta02745a

electrolytes and severe corrosion of the practical devices due to the high pH value can be effectively alleviated is still challenging but is in high demand.

Despite the active and durable electrocatalysts, the performance of a HER/OER bifunctional system is also strongly determined by the efficient assembly of electrodes.[27] During the conventional electrode fabrication, it is unavoidable to use significant fractions of inactive additives such as polymeric binders and conductive supports. These inactive additives not only increase the complexity and cost but also significantly sacrifice the electrode performance.[28,29] Although excellent electrocatalytic performance is often achieved using some novel materials for thin-layer electrodes, especially during single-electrode testing, a dramatic decay is usually unavoidable within thick electrodes for practical applications. Such a phenomenon mainly results from the increase of interfacial resistance, insufficient mass transfer, and loss of catalytic activity due to the weakly bound active materials and supports.[30] By comparison, a robust and porous three-dimensional (3D) structured electrode with a densely loaded catalyst ensures fast access to active sites, excellent catalyst-electrode contact and sufficient gas exchange channels, enabling high performance electrodes with high electrocatalytic activity and durability.[31,32]

Natural green plants have evolved with unique patterns of growth for enhanced transport phenomenon and photosynthesis reaction (Scheme 1A).[33] Inspired by their morphologies and structures, we demonstrate a novel architecture design for the development of bifunctional electrodes with a biomimetic structure at the microscopic level and with freestanding and flexible functionalities at the macroscopic level. Such 3D electrodes are densely loaded with ultralong single-crystal Co-doped ZnO nanowires *in situ* grown on highly conductive and flexible carbon fabric substrates (Co–ZnO@CF). Transition metal oxides have been widely reported with relatively strong electrocatalytic activity for the OER process, but limited activity for the HER process. The significance of this work lies in that we discover the possibility of utilizing transition metal oxides as bifunctional electrochemical catalysts, and that we purposely combine the novel transition metal oxide-based electrode materials and the efficient electrode architecture design. As illustrated in Scheme 1B, our unique electrode architecture design possesses several features[34–36] favoring the direct electrochemical water-splitting process over conventionally fabricated electrodes: (i) the ultralong one-dimensional (1D) Co-doped ZnO (Co–ZnO) nanowires with a single-crystal nature provide more active sites preferably exposed and facilitate the charge transport leading to exceptional electrocatalytic activity for both HER and OER processes in a mild alkaline system; (ii) the intimate contact between highly active nanowires and the highly conductive carbon fabric substrate ensures efficient electron transfer, while the porous structure that stemmed from the ultralong nanowires with low dimension and the 3D woven architecture of the carbon fabric provides abundant active sites for electrochemical reactions and sufficient gas exchange channels; (iii) the chemically stable substrate and robust electrode architecture significantly enhance the electrode durability. In addition, in contrast to traditional electrode structures, the 3D porous architecture enables high mass loading of active materials without performance decay. These thick electrodes are used as electrocatalysts for both anode and cathode in an overall water electrolyzer; a current density of 1.2 mA cm^{-2} at 1.7 V and 10 mA cm^{-2} at 2.0 V, as well as long-term durability (over 30 h) can be achieved, holding great promise for practical applications.

Results and discussion

Synthesis and morphology of the Co–ZnO@CF composite electrodes

The composite electrodes were prepared in a hydrothermal system with carbon fabric as the substrate (Fig. 1A). The nanowires were hydrothermally grown on the substrate, and no post-annealing process was needed after this facile one-pot synthesis. After the hydrothermal *in situ* growth, the woven

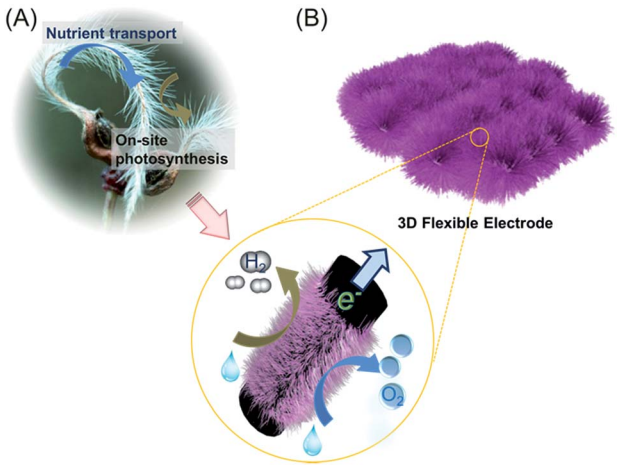

Scheme 1 (A) Hierarchical 3D structure and growth pattern of green bristlegrass in nature. (B) A schematic illustration of the biomimetic design and hydrothermal synthesis of a self-supported, flexible composite electrode with a 3D hierarchically porous architecture.

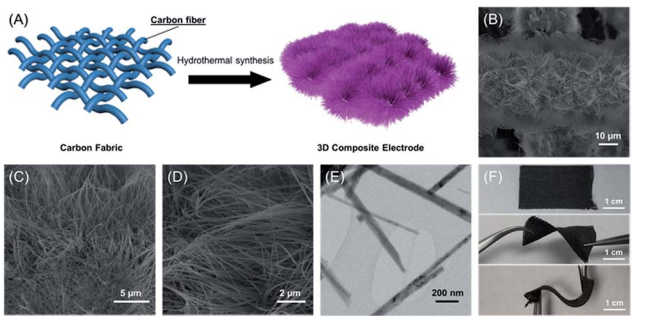

Fig. 1 (A) A schematic illustration of the hydrothermal synthesis of the self-supported, flexible composite electrode with the 3D hierarchically porous architecture. (B and C) Low-magnification SEM image of the 3D electrode. (D) High-magnification SEM image of ultralong nanowires *in situ* grown on carbon fibers. (E) TEM image of the nanowires. (F) Digital photos of the composite electrode in the relaxed, twisted and bent states.

structure of the carbon fabric (Fig. S1†) is fully maintained, while the texture architecture is well established, which is revealed by the representative scanning electron microscopy (SEM) image (Fig. 1B). It can be found that one-dimensional (1D) nanowires are formed, which evenly and tightly cover the carbon fibers from the carbon fabric. Obviously, such a pattern of growth endows the electrode with a preferred 3D hierarchically porous composite structure (Fig. 1C) favoring electrolyte diffusion and gas exchange. Some nanowire clusters can also be observed, which are mainly attributed to the high nanowire loading density.[37]

The high-magnification SEM image in Fig. 1D reveals that these nanowires possess relatively uniform diameters with a length of at least tens of microns, exhibiting their ultralong nature. In addition, some of the curly parts of these nanowires indicate their lithe nature. The representative transmission electron microscopy (TEM) image further depicts that these NWs possess uniform diameters of approximately 50 nm (Fig. 1E), with a large aspect ratio and smooth surface along the entire nanowires, implying a highly single crystal nature. Obviously, such an architecture of composite electrodes is expected to well accommodate any spatial and structural changes and to enable a robust electrode, while the high active-surface area and binder-free interface between the 1D ultralong NWs and highly conductive carbon fibers further benefit fast ion and electron transfer.[38] The photographic images of a piece of the composite electrode (Fig. 1F) show that the composite electrode can be either bent or twisted, or even readily rolled up periodically, exhibiting excellent flexibility and making it possible for further flexible device applications.

Structure and composition of the ultralong single-crystal Co–ZnO nanowires

In order to analyze the constitution of the active material, energy-dispersive X-ray spectroscopy (EDS) was performed on the 1D ultralong nanowires. Fig. 2A shows the representative EDS elemental mapping on a fraction of a single nanowire. It can be found that only the elements Zn, Co, and O are present and homogeneously distributed along the 1D structure, implying the formation of Co–Zn–O based nanowires. The signal intensity of the element Co is significantly weaker than that of the element Zn, indicating its low content ratio in the Co–Zn–O nanowires. It is worth mentioning that it is impossible to realize *in situ* growth of pure ZnO on carbon fabric under the identical reaction conditions without using the cobalt precursor, while pure Co_3O_4 is able to grow on carbon fabric, however, only with a shorter length, forming a rod-like morphology (Fig. S2†). The X-ray diffraction (XRD) pattern (Fig. S3†) shows a clear hexagonal crystal structure, which can be indexed to zincite ZnO (JCPDS no. 01-1136). No obvious peaks can be observed for $ZnCo_2O_4$ and other Co and Zn based oxide impurities, suggesting the formation of ZnO nanowires with Co doping. Compared to the $ZnCo_2O_4$ nanowires with a polycrystalline structure, such a homogeneous elemental distribution as well as the XRD pattern implies the formation of single crystals. Fig. 2B shows two nanowires leaning on each other and exhibiting a sleek surface along the entire 1D direction, which is completely different from the reported $ZnCo_2O_4$ nanowires with a polycrystalline structure.[39–41] The single-crystal nature can be further confirmed by high-resolution TEM (HRTEM) images. As shown in Fig. 2C and D, both the bulk and edge areas (boxed in Fig. 2B) of a single nanowire possess clear and continuous fringes with a lattice spacing of ~0.52 nm, which can be indexed to the (001) plane in the typical hexagonal structure of ZnO and is consistent with XRD analysis. The slight lattice spacing difference can be attributed to the slight doping concentration of the element Co. The highly single crystalline nature can be further revealed by the FFT diffraction pattern (Fig. S4†), with an unusual (001) plane

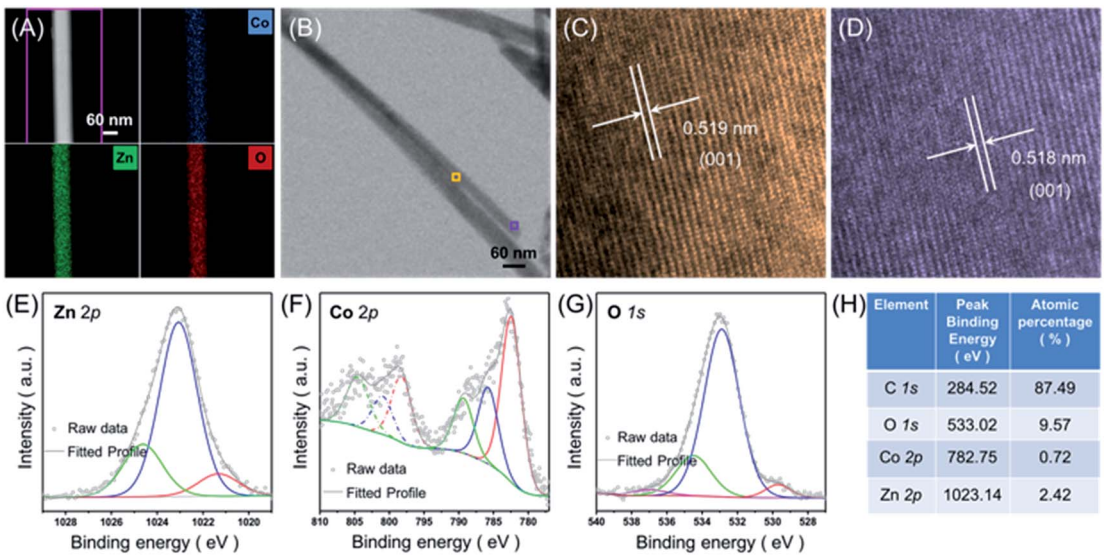

Element	Peak Binding Energy (eV)	Atomic percentage (%)
C 1s	284.52	87.49
O 1s	533.02	9.57
Co 2p	782.75	0.72
Zn 2p	1023.14	2.42

Fig. 2 (A) HAADF-STEM image of a randomly selected area from a single nanowire and the corresponding elemental mapping spectra on Zn, Co, and O. (B) TEM image of two nanowires next to each other. (C and D) HRTEM images of the nanowire within the boxed areas. Core-level scan XPS spectrum of elements (E) Zn, (F) Co and (G) O in the composite electrode. (H) Elemental ID and quantification from XPS analysis.

preferentially exposed, which is consistent with the HRTEM observation and may lead to a significantly enhanced catalytic activity.

The composition and oxidation states are further analyzed by X-ray photoelectron spectroscopy (XPS), which also confirms the existence of the elements Zn, Co and O, and a significant amount of the element C from the carbon fabric substrate (Fig. S5†). As shown in Fig. 2E, the core-level XPS spectra of the element Zn can be interpreted from three major peaks at 1024.65, 1023.08 and 1021.31 eV, which can be attributed to Zn atoms with different configurations and non-stoichiometry.[42,43] Fig. 2F displays the high-resolved spectrum of Co 2p exhibiting two strong peaks for Co $2p_{1/2}$ and $2p_{3/2}$, with an energy gap of ~15.7 eV, confirming the presence of the element Co. Both Co $2p_{1/2}$ and $2p_{3/2}$ spectra can be deconvoluted into three Gaussian peaks. The major peak located at 782.55 eV can be ascribed to Co(II) oxidation states, indicating that the doped Co exists in ZnO nanowires mainly in the Co^{2+} state.[44,45] In addition, two minor peaks at a higher energy region suggest the presence of a small amount of Co in a higher oxidation state, which is not avoidable during the synthesis.[46] Fig. 2G shows the O 1s spectrum with a single peak, which can be fitted into four Gaussian peaks. The major peak located at 532.90 eV is attributed to the O^{2-} ion in the Zn–O bonding of ZnO. The two shoulder peaks at the higher energy region correspond to the chemisorbed oxygen related to the Co doping.[47] Interestingly, the shoulder peak located at the lower energy region indicates the lower oxidation state of the element O, implying the existence of a small amount of Co^{3+}, which also agrees with the Co spectrum analysis. The composition of Co–ZnO nanowires is also analyzed by XPS results. As shown in Fig. 2H, the element Co possesses a remarkably high atomic percentage of ~0.72% in the whole composite electrode, corresponding to an atomic percentage of ~13% in the single crystal nanowires.[48,49]

Electrocatalytic performance of the Co–ZnO@CF composite electrodes

The self-supported Co–ZnO@CF composite electrode possesses novel material morphology and a unique 3D architecture for improved catalytic performance. The electrocatalytic performance was first evaluated by the steady-state linear sweep voltammetry (LSV) technique in a three-electrode system, where the self-supported composite electrode served directly as the working electrode, a Pt wire as the counter electrode and a saturated calomel electrode (SCE) as the reference electrode. It is worth emphasizing that a N_2-saturated mild alkaline solution (0.1 M KOH aqueous solution) was used as the electrolyte rather than a strong basic solution (1.0 M KOH) which often gives much better performance but is not practically compatible.[7] Fig. 3A compares the polarization curves of the Co–ZnO@CF, Co_3O_4/CF composite electrodes and carbon fabric with that of the Ir/C benchmark for the OER process at a scan rate of 10 mV s^{-1}. Obviously, the pure carbon fabric doesn't show any current toward OER, as expected, while the commercial Ir/C catalyst exhibits a low onset potential and requires an overpotential of 386 mV to reach a current density of 20 mA cm^{-2}, indicating its excellent catalytic activity. By comparison, the Co_3O_4/CF composite electrode exhibits a lower onset potential and an overpotential of 423 mV to reach a current density of 10 mA cm^{-2}, and 475 mV to reach 20 mA cm^{-2}. Remarkably, the Co–ZnO/CF composite electrode shows a comparable onset potential to that of the Co_3O_4/CF composite electrode and Ir/C catalyst but only requires a small overpotential of 360 mV to reach a current density of 10 mA cm^{-2} and 380 mV to reach 20 mA cm^{-2}. Moreover, it exhibits a steep current increase and only needs an extremely low overpotential of 414 mV to achieve a high current of 50 mA cm^{-2}, which significantly outperforms the commercial Ir/C catalyst. Such outstanding OER electrocatalytic performance is also revealed by the Tafel analysis, where the slope of the Co–ZnO/CF composite electrode is comparable to that of the commercial Ir/C catalyst (68 mV dec^{-1} *vs.* 67 mV dec^{-1}) (Fig. 3B). To the best of our knowledge, the OER performance of Co–ZnO/CF is among the best of all reported literature studies. It is not only superior to that of some non-precious metal OER catalysts in mild alkaline media, but also surprisingly better than some materials tested in a strong (1.0 M KOH) electrolyte, which is summarized in Table S1.†

Interestingly, in addition to the OER electrocatalytic activity, the composite electrodes also show relatively strong HER electrocatalytic performance, which is not commonly observed for most transition metal oxides. As shown in Fig. 4A, the pure carbon fabric doesn't show appreciable current toward the HER process, implying its ignorable electrocatalytic activity. The Pt/C catalyst requires an overpotential of 16 mV to reach a current

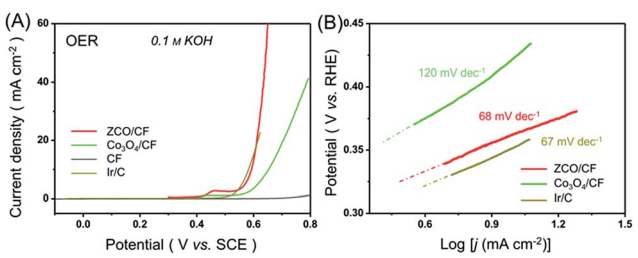

Fig. 3 (A) OER polarization curves of the Co–ZnO/CF, Co_3O_4/CF composite electrodes compared with the Ir/C benchmark, at a scan rate of 10 mV s^{-1} in 0.1 M KOH electrolyte. (B) OER Tafel plots of the Co–ZnO/CF, Co_3O_4/CF composite electrodes compared with the Ir/C benchmark.

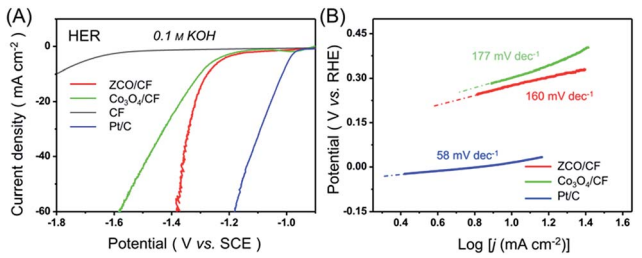

Fig. 4 (A) HER polarization curves of the Co–ZnO/CF, Co_3O_4/CF composite electrodes compared with the Pt/C benchmark, at a scan rate of 10 mV s^{-1} in 0.1 M KOH electrolyte. (B) HER Tafel plots of the Co–ZnO/CF, Co_3O_4/CF composite electrodes compared with the Pt/C benchmark.

density of 10 mA cm^{-2}. By comparison, the polarization curves indicate that overpotentials of 275 and 302 mV are required to reach 10 mA cm^{-2}, and 328 and 398 to reach a current density of 25 mA cm^{-2}, for Co–ZnO/CF and Co_3O_4/CF composite electrodes, respectively. Although the Pt/C commercial catalyst shows a considerably lower onset potential, the Co–ZnO/CF composite electrode exhibits a drastically increased current density, indicating fast electrode kinetics stemming from both fast redox reactions and efficient mass transport. Remarkably, a high current density of 50 mA cm^{-2} for Co–ZnO/CF can be achieved at a small overpotential of only 360 mV. Similarly, such a good HER electrocatalytic activity of the Co–ZnO/CF composite electrode is comparable or superior to that of many HER catalysts in either mild or strong alkaline media, which is summarized in Table S2.† We believe that the reasonable HER electrocatalytic activity is mainly due to the Co doping which shows mixed valence states revealed by the XPS analysis in Fig. 2F. Note that there are only few literature studies reporting the HER catalytic activities of transition metal oxides, which limit the use of transition metal oxides as bifunctional electrocatalysts for overall water splitting.

Such outstanding bifunctional electrocatalytic performance of the Co–ZnO/CF composite electrode is clearly observed when compared with various electrodes. Noticeably, the self-supported 3D Co–ZnO/CF composite electrode can afford a current density of 20 mA cm^{-2} at a much lower overpotential than that of the commercial Ir/C catalyst, and a current density of 50 mA cm^{-2} at a reasonable overpotential to that of the commercial Pt/C catalyst (Fig. 5A). We believe that the outstanding activity is mainly attributed to the novel morphology of the electrocatalytic materials and the unique 3D porous electrode architecture, where the mass transfer and electrical conductivity are both greatly enhanced. Note that the Pt/C (28 wt%) and Ir/C (20 wt%) catalysts were loaded onto a glassy carbon (GC) electrode and the carbon fabric (CF) with the same loading mass of 1.0 mg cm^{-2} (Fig. S6†), respectively, for comparison. Both Pt/C and Ir/C catalysts loading on GC showed much better catalytic activities than on CF. In practical applications, higher loading mass and larger pieces of electrodes are often required. In this context, our composite electrode with the unique 3D porous architecture enabling high mass loading without sacrificing the catalytic performance is highly favorable. In addition to the superior electrocatalytic activity, the 3D porous Co–ZnO/CF composite electrode also exhibits significantly improved durability. As shown in Fig. 5B, after 3000 cycles of cyclic voltammetry (CV) at a high scan rate of 50 mV s^{-1}, a small overpotential shift of 45 mV for HER and 19 mV for OER is obtained to reach a current density of 20 mA cm^{-2} under LSV. Such durability is further revealed by the SEM image of the composite electrode where both the ultralong 1D nanowire morphology and the biomimetic composite architecture are well maintained (Fig. 5C and D).

Building on the promising electrochemical activity and durability of the Co–ZnO/CF composite electrode, we further explored the feasibility of such a 3D self-supported composite electrode to be used in a full device for future practical applications. As shown in Fig. 6A, a single-cell of a direct water-splitting system was assembled using the Co–ZnO/CF composite electrodes as both the cathode and anode. This electrolyzer requires a slightly higher initial cell voltage of 2.02 V to reach the current of 10 mA cm^{-2} for water-splitting in a mild alkaline electrolyte (Fig. 6B). However, it shows an interesting increase of the electrochemical catalytic activity and exceptional stability. As shown in Fig. 6C, it can be found that the catalysis process starts at 2.00 V to deliver a current

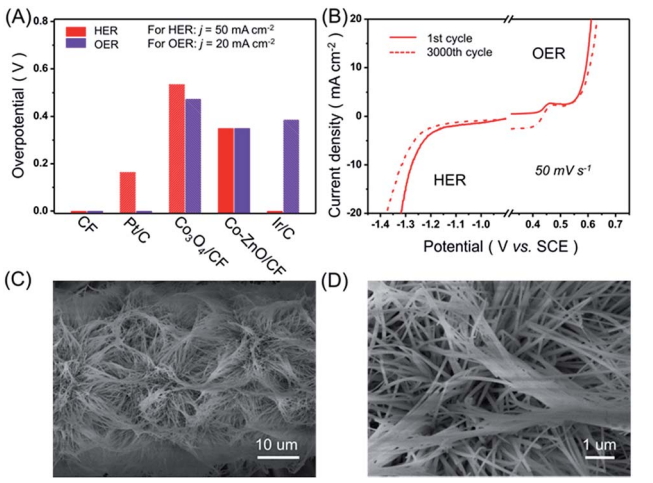

Fig. 5 (A) Specific activities of different electrodes in 0.1 M KOH electrolyte at 50 mA cm^{-2} for HER and 20 mA cm^{-2} for OER. (B) HER and OER polarization curves of the Co–ZnO/CF composite electrode before and after 3000 cycles. Corresponding (C) low- and (D) high-magnification SEM images of the surface of the Co–ZnO/CF composite electrode after 3000 cycles.

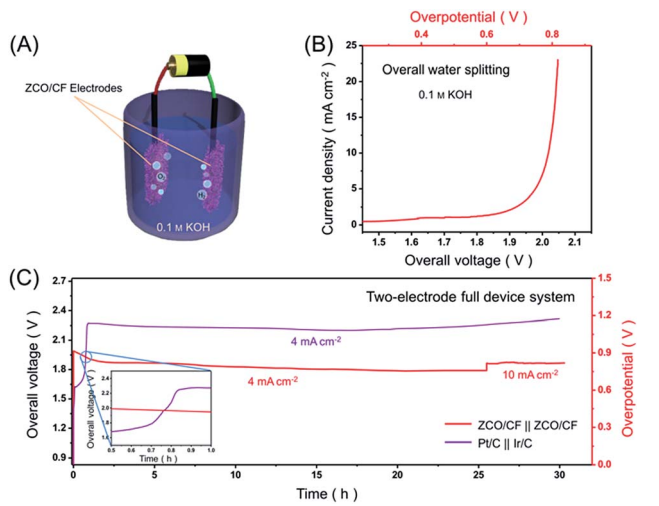

Fig. 6 (A) A schematic illustration of the two-electrode water splitting system using 3D Co–ZnO/CF composite electrodes as both the anode and cathode. (B) Co–ZnO/CF composites as HER and OER bifunctional electrodes in 0.1 M KOH aqueous solution electrolyte for overall water splitting. (C) Comparison of the long-term stability of two-electrode full water splitting systems. An activation process occurs when an electrolysis current density of 4 mA cm^{-2} is applied followed by a stable overall voltage for long-term continuous operation. As a sharp contrast, a full water splitting system composing Ir/C and Pt/C based catalytic electrodes shows dramatic performance decay.

density of 4.0 mA cm^{-2}, while the cell voltage quickly drops to around 1.9 V and maintains for 25 hours. Even when the current density increases to 10.0 mA cm^{-2}, the cell voltage still remains stable at a low voltage of 2.06 V. By comparison, although a counterpart system consisting of the Pt/C catalyst anode and Ir/C catalyst cathode shows a low starting cell voltage of 1.69 V during a direct electrochemical water splitting, the electrocatalytic performance dramatically decreases after less than 1 h with the overall voltage increasing to ~2.3 V at a current density of 4.0 mA cm^{-2}. This phenomenon further implies outstanding electrocatalytic activity and impressive durability of the Co–ZnO/CF composite electrodes.

Conclusions

In summary, we have successfully designed and fabricated a 3D porous and flexible electrode based on ultralong Co-doped ZnO single crystal nanowires *in situ* grown on a highly conductive carbon fabric substrate for efficient direct water splitting. Such an electrode shows excellent electrochemical catalytic activity and durability owing to the novel materials and unique electrode architecture, where both mass transport as well as electron conductivity and redox reactions are significantly enhanced. The single-cell prototype using such electrodes exhibits superior performance including low overall voltage and extremely long durability to noble metal-based catalyst counterparts, which holds great promise in future practical applications.

Experimental

Fabrication of composite electrodes

Carbon fabric (CF) was cleaned using water, acetone and ethanol with ultrasonication for 30 min each to remove impurities before it was surface-functionalized using concentrated HNO_3 (65 wt%) at room temperature overnight and washed with distilled & deionized (DDI) water and dried under vacuum at 80 °C for 8 hours. In a typical fabrication of the Co–ZnO/CF composite electrode, $Zn(NO_3)_2 \cdot 6H_2O$ (0.446 g), $Co(NO_3)_2 \cdot 6H_2O$ (1.0914 g), urea (0.225 g), and NH_4F (0.056 g) were completely dissolved in DDI water (30 mL) under stirring until the solution turned transparent. One piece of CF (5.0 cm × 5.0 cm) was placed into the solution under ultrasonication for 30 min. Then the solution and CF were transferred together into a 50 mL Teflon-lined autoclave, and kept at 180 °C for 10 h. After the hydrothermal process, the obtained CF was rinsed with DDI water and ethanol repeatedly, and dried in vacuum at 80 °C overnight. The Co_3O_4/CF composite electrode was fabricated using the same procedure without adding $Co(NO_3)_2 \cdot 6H_2O$. Detailed experiments, material characterization and electrochemical measurements can be found in the ESI.†

Acknowledgements

The authors would like to acknowledge the financial support from the Natural Sciences and Engineering Research Council of Canada (NSERC), the University of Waterloo, and the Waterloo Institute for Nanotechnology. The authors also acknowledge the assistance from the Canadian Center for Electron Microscopy (CCEM) at McMaster University for TEM and HAADF-STEM characterization. The authors also thank Dr Min Ho Seo for the physicochemical analysis by the framework of research and development program of KIER (B6-2425).

Notes and references

1 M. G. Walter, E. L. Warren, J. R. McKone, S. W. Boettcher, Q. Mi, E. A. Santori and N. S. Lewis, *Chem. Rev.*, 2010, **110**, 6446–6473.
2 M. S. Dresselhaus and I. L. Thomas, *Nature*, 2001, **414**, 332–337.
3 C. Liu, J. Tang, H. M. Chen, B. Liu and P. Yang, *Nano Lett.*, 2013, **13**, 2989–2992.
4 H. B. Gray, *Nat. Chem.*, 2009, **1**, 7.
5 Y. Lee, J. Suntivich, K. J. May, E. E. Perry and Y. Shao-Horn, *J. Phys. Chem. Lett.*, 2012, **3**, 399–404.
6 J. Wang, W. Cui, Q. Liu, Z. Xing, A. M. Asiri and X. Sun, *Adv. Mater.*, 2016, **28**, 215–230.
7 H. Wang, H.-W. Lee, Y. Deng, Z. Lu, P.-C. Hsu, Y. Liu, D. Lin and Y. Cui, *Nat. Commun.*, 2015, **6**, 7261.
8 K. Zeng and D. Zhang, *Prog. Energy Combust. Sci.*, 2010, **36**, 307–326.
9 G. Li, X. Wang, J. Fu, J. Li, M. G. Park, Y. Zhang, G. Lui and Z. Chen, *Angew. Chem., Int. Ed.*, 2016, **55**, 4977–4982.
10 C. C. L. McCrory, S. Jung, J. C. Peters and T. F. Jaramillo, *J. Am. Chem. Soc.*, 2013, **135**, 16977–16987.
11 Y. Jiao, Y. Zheng, M. Jaroniec and S. Z. Qiao, *Chem. Soc. Rev.*, 2015, **44**, 2060–2086.
12 D. U. Lee, P. Xu, Z. P. Cano, A. G. Kashkooli, M. G. Park and Z. Chen, *J. Mater. Chem. A*, 2016, **4**, 7107–7134.
13 M. W. Kanan and D. G. Nocera, *Science*, 2008, **321**, 1072–1075.
14 J. Suntivich, K. J. May, H. A. Gasteiger, J. B. Goodenough and Y. Shao-Horn, *Science*, 2011, **334**, 1383–1385.
15 A. Grimaud, K. J. May, C. E. Carlton, Y.-L. Lee, M. Risch, W. T. Hong, J. Zhou and Y. Shao-Horn, *Nat. Commun.*, 2013, **4**, 2439.
16 F. Cheng, J. Shen, B. Peng, Y. Pan, Z. Tao and J. Chen, *Nat. Chem.*, 2011, **3**, 79–84.
17 M. Gong, Y. Li, H. Wang, Y. Liang, J. Z. Wu, J. Zhou, J. Wang, T. Regier, F. Wei and H. Dai, *J. Am. Chem. Soc.*, 2013, **135**, 8452–8455.
18 J. R. McKone, B. F. Sadtler, C. A. Werlang, N. S. Lewis and H. B. Gray, *ACS Catal.*, 2013, **3**, 166–169.
19 W.-F. Chen, K. Sasaki, C. Ma, A. I. Frenkel, N. Marinkovic, J. T. Muckerman, Y. Zhu and R. R. Adzic, *Angew. Chem., Int. Ed.*, 2012, **51**, 6131–6135.
20 X. Zou, X. Huang, A. Goswami, R. Silva, B. R. Sathe, E. Mikmeková and T. Asefa, *Angew. Chem., Int. Ed.*, 2014, **53**, 4372–4376.
21 J. Wang, D. Gao, G. Wang, S. Miao, H. Wu, J. Li and X. Bao, *J. Mater. Chem. A*, 2014, **2**, 20067–20074.
22 D. Voiry, H. Yamaguchi, J. Li, R. Silva, D. C. B. Alves, T. Fujita, M. Chen, T. Asefa, V. B. Shenoy, G. Eda and M. Chhowalla, *Nat. Mater.*, 2013, **12**, 850–855.

23 M. A. Lukowski, A. S. Daniel, F. Meng, A. Forticaux, L. Li and S. Jin, *J. Am. Chem. Soc.*, 2013, **135**, 10274–10277.
24 E. J. Popczun, J. R. McKone, C. G. Read, A. J. Biacchi, A. M. Wiltrout, N. S. Lewis and R. E. Schaak, *J. Am. Chem. Soc.*, 2013, **135**, 9267–9270.
25 J. Masa, P. Weide, D. Peeters, I. Sinev, W. Xia, Z. Sun, C. Somsen, M. Muhler and W. Schuhmann, *Adv. Energy Mater.*, 2016, **6**, 1502313.
26 Y. Tan, H. Wang, P. Liu, Y. Shen, C. Cheng, A. Hirata, T. Fujita, Z. Tang and M. Chen, *Energy Environ. Sci.*, 2016, **9**, 2257–2261.
27 H. M. Chen, C. K. Chen, R.-S. Liu, L. Zhang, J. Zhang and D. P. Wilkinson, *Chem. Soc. Rev.*, 2012, **41**, 5654–5671.
28 T. Y. Ma, J. Ran, S. Dai, M. Jaroniec and S. Z. Qiao, *Angew. Chem., Int. Ed.*, 2015, **54**, 4646–4650.
29 D. Kong, H. Wang, Z. Lu and Y. Cui, *J. Am. Chem. Soc.*, 2014, **136**, 4897–4900.
30 J. Fu, F. M. Hassan, J. Li, D. U. Lee, A. R. Ghannoum, G. Lui, M. A. Hoque and Z. Chen, *Adv. Mater.*, 2016, **28**(30), 6421–6428.
31 S. Chen and S.-Z. Qiao, *ACS Nano*, 2013, **7**, 10190–10196.
32 Y.-H. Chang, F.-Y. Wu, T.-Y. Chen, C.-L. Hsu, C.-H. Chen, F. Wiryo, K.-H. Wei, C.-Y. Chiang and L.-J. Li, *Small*, 2014, **10**, 895–900.
33 R. Wang, D. C. Higgins, D. U. Lee, S. Prabhudev, F. M. Hassan, V. Chabot, G. Lui, G. Jiang, J.-Y. Choi, L. Rasenthiram, J. Fu, G. Botton and Z. Chen, *Nano Energy*, 2016, **20**, 57–67.
34 X. Wang, G. Li, F. M. Hassan, M. Li, K. Feng, X. Xiao and Z. Chen, *J. Mater. Chem. A*, 2015, **3**, 3962–3967.
35 X. Wang, G. Li, Z. Chen, V. Augustyn, X. Ma, G. Wang, B. Dunn and Y. Lu, *Adv. Energy Mater.*, 2011, **1**, 1089–1093.
36 X. Wang, G. Li, M. H. Seo, F. M. Hassan, M. A. Hoque and Z. Chen, *Adv. Energy Mater.*, 2015, **5**, 1501106.
37 B. Guan, D. Guo, L. Hu, G. Zhang, T. Fu, W. Ren, J. Li and Q. Li, *J. Mater. Chem. A*, 2014, **2**, 16116–16123.
38 B. Liu, J. Zhang, X. Wang, G. Chen, D. Chen, C. Zhou and G. Shen, *Nano Lett.*, 2012, **12**, 3005–3011.
39 S. Wang, J. Pu, Y. Tong, Y. Cheng, Y. Gao and Z. Wang, *J. Mater. Chem. A*, 2014, **2**, 5434–5440.
40 B. Qu, L. Hu, Q. Li, Y. Wang, L. Chen and T. Wang, *ACS Appl. Mater. Interfaces*, 2014, **6**, 731–736.
41 B. Liu, B. Liu, Q. Wang, X. Wang, Q. Xiang, D. Chen and G. Shen, *ACS Appl. Mater. Interfaces*, 2013, **5**, 10011–10017.
42 Z. Li and L. Yin, *J. Mater. Chem. A*, 2015, **3**, 21569–21577.
43 J. Bai, X. Li, G. Liu, Y. Qian and S. Xiong, *Adv. Funct. Mater.*, 2014, **24**, 3012–3020.
44 S. Vempati, A. Shetty, P. Dawson, K. K. Nanda and S. B. Krupanidhi, *Thin Solid Films*, 2012, **524**, 137–143.
45 V. Gandhi, R. Ganesan, H. H. Abdulrahman Syedahamed and M. Thaiyan, *J. Phys. Chem. C*, 2014, **118**, 9715–9725.
46 T. W. Kim, M. A. Woo, M. Regis and K.-S. Choi, *J. Phys. Chem. Lett.*, 2014, **5**, 2370–2374.
47 D. Wan, F. Huang, Y. Wang, X. Mou and F. Xu, *ACS Appl. Mater. Interfaces*, 2010, **2**, 2147–2152.
48 T. R. Paudel, S. Lany, M. d'Avezac, A. Zunger, N. H. Perry, A. R. Nagaraja, T. O. Mason, J. S. Bettinger, Y. Shi and M. F. Toney, *Phys. Rev. B: Condens. Matter Mater. Phys.*, 2011, **84**, 064109.
49 T. R. Paudel, A. Zakutayev, S. Lany, M. d'Avezac and A. Zunger, *Adv. Funct. Mater.*, 2011, **21**, 4493–4501.